RSC Advances

PAPER

View Article Online
View Journal | View Issue

Cite this: *RSC Adv.*, 2024, **14**, 5149

A phenothiazine-functionalized pyridine-based AIEE-active molecule: a versatile molecular probe for highly sensitive detection of hypochlorite and picric acid†

Dhandapani Vinayagam and Karpagam Subramanian *

Received 11th December 2023
Accepted 31st January 2024

DOI: 10.1039/d3ra08451e

rsc.li/rsc-advances

In this study, we designed and synthesized a novel compound (**PTH-AB-PY**) based on phenothiazine and pyridine moieties with aggregation-induced emission enhancement (AIEE) properties. The compound has shown exceptional selectivity and sensitivity towards ClO^- ions with an impressive detection limit of 6.86×10^{-4} M. Its remarkable sensitivity arises from its effective inhibition of the photoinduced electron transfer (PET) mechanism. Job's plot analysis and high-resolution mass spectrometry (HR-MS) confirmed the 1 : 1 binding ratio between the compound and ClO^-. The synthesized compound also exhibits higher sensitivity and fluorescence quenching towards the explosive species (picric acid), with a detection limit of around 1.44×10^{-6} M. Furthermore, our work was carried out for real-time water sample analysis to check ClO^- and picric acid detection and high recovery rates (94 to 99%) were achieved. These findings highlight the potential of **PTH-AB-PY** as a promising molecular probe for ClO^- ions and picric acid detection with various analytical and environmental applications.

Introduction

Hypochlorite (ClO^-) plays a crucial role in biological processes by acting as a reactive oxygen species, particularly within the immune system, to combat invading bacteria.[1,2] However, elevated levels of ClO^- can lead to conditions such as cancer, pulmonary fibrosis, and neurodegenerative disorders due to oxidative stress.[3,4] Monitoring ClO^- levels is vital for disease diagnosis and environmental safety in drinking water, sewage, and swimming pools. Sodium hypochlorite and hypochlorous acid are the primary sources of hypochlorite. On the other hand, picric acid poses hazards due to its toxicity and explosive properties. Proper storage and transportation of picric acid are essential to prevent environmental contamination and safeguard public health.[5–7] Contact with picric acid may result in skin irritation, allergic responses, severe burns, or damage to internal organs.[8,9] Disposal methods should comply with safety guidelines involving neutralization, chemical decomposition, and specialized hazardous waste management facilities.[10–12]

Sensing technologies are crucial in identifying metals, anions, and nitro aromatics, serving essential functions across various sectors, such as environmental monitoring, healthcare, industrial processes, and security. Accurate detection and quantification of these substances is essential to ensure safety and compliance with regulatory standards and facilitate scientific research. Among the sensing methodologies, fluorescent sensing offers an easy way to identify analytes using turn-on and turn-off mechanisms. Additionally, changes in fluorescence colour demonstrate the interaction of analytes. Fluorescent probes have gained popularity in recognizing ClO^- and picric acid due to their precision, low limits of detection,[13,14] user-friendly nature, and ability to provide visual indicators.[15,16] Furthermore, compounds such as pyrenes and porphyrin dyes[17,18] have markedly enhanced sensitivity and selectivity in sensing anions. Conjugated polymer films and electrodes accurately measure anions in real-time through electrochemical sensing.[19,20] These technologies are promising for various analytical[21–23] and environmental applications.[24–26] Meanwhile, anion-responsive ligand-functionalized conjugated nanoparticles provide accurate and sensitive anion detection mechanisms through fluorescence quenching or enhancement mechanisms.[27,28]

Phenothiazine-based conjugated compounds exhibit high sensing performance due to their strong fluorescence properties,[29–31] and the sulfur atom shows the interaction ability towards anions like ClO^-. The compounds which contain nitrogen heteroatoms have shown interactions with picric acid.[32–34] Additionally, achieving sensitivity in aqueous environments remains challenging due to picric acid's limited solubility in water.[35,36] Efforts are underway to improve detection in aqueous solutions. Furthermore, there are limitations in achieving ultra-low detection limits, maintaining stability, and ensuring long-term performance.

Department of Chemistry, School of Advanced Sciences, Vellore Institute of Technology, Vellore, 632014, Tamil Nadu, India. E-mail: skarpagam80@yahoo.com; skarpagam@vit.ac.in; Tel: +91-416-2202334. Fax: +91-416-2243092

† CCDC 2278692. For crystallographic data in CIF or other electronic format see DOI: https://doi.org/10.1039/d3ra08451e

This study introduces a newly developed probe (**PTH-AB-PY**) specifically for sensing ClO^- and picric acid. The phenothiazine sulfur atom functions as the recognition site for hypochlorite, while pyridine serves as the fluorophore, acting as a turn-off sensor for picric acid. The detection mechanism relies on the oxidation of the sulfur atom by highly reactive oxygen species (hROS), enabling specific interaction towards ClO^-. Furthermore, the nitrogen within the pyridine moiety significantly influences the scientific identification of picric acid. Notably, this probe can selectively interact with ClO^- ions and picric acid in real-time samples within 2 seconds, even in water and vegetable samples. By effectively addressing solubility challenges and harnessing fluorescence enhancements, this probe shows promising potential for accurately identifying ClO^- and picric acid in aqueous environments.

Materials and methods

Reagents and solvents

The chemicals used in this study, such as phenothiazine, allyl bromide, 2-pyridyl acetonitrile, and phosphorus oxychloride, were purchased from Sigma-Aldrich in Bangalore. Solvents, including dimethylformamide, chloroform, acetonitrile, acetone, tetrahydrofuran, hexane, and ethyl acetate, were purchased from Avra and used without further purification.

Characterization techniques

The NMR spectra were obtained using a Bruker spectrometer operating at 400 MHz, and the chemical shifts (δ) were reported in parts per million (ppm) relative to Me_4Si for both ^1H and ^{13}C NMR. FT-IR spectra were obtained by preparing KBr discs and analyzing them using a Shimadzu FT-IR spectrometer within the 400–4000 cm^{-1} range. High-resolution mass spectrometry (HRMS) analysis was performed using a WATER-XEVO G2XS-QT instrument. Absorption spectra were recorded with an Agilent 8453 UV-visible diode array spectrophotometer, using acetonitrile as the solvent. Fluorescence spectra were obtained using an Edinburgh FLS 980 spectrometer for steady-state photoluminescence studies. Visual observation of changes in aggregation was facilitated using a scanning electron microscope, specifically the THERMO FISHER FEI-QUANTA 250 FEG model.

Sample preparation for sensing

A stock solution of **PTH-AB-PY** (1×10^{-4} mol l^{-1}) was prepared in acetonitrile solvent. ClO^- was generated by dissolving NaClO in water (0.1 mol l^{-1}). Stock solutions (0.1 mol l^{-1}) of various anions (Cl^-, F^-, COO^-, HCO_3^-, HSO_4^-, I^-, CO_3^{2-}, SO_3^{2-}, Br^-, HPO_4^-, NO_3^-, OH^-) were prepared using distilled water. Stock solutions of various nitro aromatics (DNP, PNP, NB, NM, and PA) at a concentration of (1×10^{-3} mol l^{-1}) were prepared using distilled water. All subsequent optical spectral characterization studies were conducted using these prepared stock solutions.

Computational calculations

This computational study has been investigated to the ligand probe **PTH-AB-PY** and its sulfone derivative S=O using Density Functional Theory (DFT) calculations performed with the G16 package. We used the B3LYP function to optimize the molecular structures of these systems. The basic structure 6-31G(d) is used for hydrogen, carbon, nitrogen, and oxygen atoms, enabling a comprehensive exploration of potential energy surfaces. Furthermore, the electronic properties were analyzed by visualizing and examining frontier molecular orbitals using Gauss View 6.1.1, providing valuable insights into molecular reactivity and interactions.

Analytical studies

Small test strips of Whatman filter paper were dipped in a ligand solution in a 1×10^{-4} M concentration and dried. Subsequently, we added an anion solution with an equal concentration to these treated paper segments, followed by another drying process. Monitoring the solid-state color changes involves utilizing silica gel with a mesh size ranging from 60 to 120. We added 2 ml of the compound and 0.5 ml of the different anions. The test strip's color changes assessed how the analytes interacted.

Experimental

Synthesis of 10-allyl-10*H*-phenothiazine (PTH-AB)

In a 100 ml round-bottom flask, 10*H*-phenothiazine (1) (3.0 g, 15 mmol) was dissolved in 40 ml DMF and cooled to 0 °C. Subsequently, sodium hydride (0.6 g, 15 mmol) was added, and the mixture was stirred at room temperature for 1 hour. Then, allyl bromide (1.3 ml, 15 mmol) was added to the reaction mixture and stirred for 12 hours. Upon completion of the reaction, the mixture was extracted with chloroform. The resultant product (**PTH-AB**) was purified by column chromatography using petroleum ether, resulting in a 70% yield of colourless liquid (3 ml). ^1H NMR ($CDCl_3$, 400 MHz, δ ppm) (Fig. S1†): 7.05 to 7.07 (m, 4H), 6.82 to 6.87 (m, 4H), 5.9 to 6.0 (m, 1H), 5.3 (d, 2H), and 4.4 (d, 2H). FT-IR (KBr, ν/cm^{-1}) (Fig. S2†): 1593, 1450, 1483.

Synthesis of 10-allyl-10*H*-phenothiazine-3-carbaldehyde (PTH-AB-1CHO)

In a 250 ml round-bottom flask, 20 ml DMF was cooled to 0 °C. Subsequently, 1.6 ml (16.4 mmol) $POCl_3$ was added and stirred for 30 minutes. Following this, 1 g (4.1 mmol) of **PTH-AB** was added, and the mixture was refluxed at 70 °C for 12 hours. The resulting reaction mixture was neutralized using sodium carbonate and water and then separated using chloroform. The compound was purified *via* column chromatography, utilizing a mixture of hexane and ethyl acetate (8 : 2) as the eluent. The final product (**PTH-AB-1CHO**), a yellow viscous liquid, was obtained with a yield of 66%. ^1H NMR ($CDCl_3$, 400 MHz, δ ppm) (Fig. S3†): 9.76 (s, 1H), 6.82 to 7.52 (m, 7H), 6.0 (m, 1H), 5.2 (d, 2H), and 4.5 (d, 2H). ^{13}C NMR ($CDCl_3$, 101 MHz, δ ppm) (Fig. S4†): 190, 119 to 152. FT-IR (KBr, ν/cm^{-1}): 1680, 2720, and 2830.

Synthesis of (*Z*)-3-(10-allyl-10*H*-phenothiazin-3-yl)-2(pyridin-2-yl) acrylonitrile (PTH-AB-PY)

In a 250 ml round bottom flask, 2-pyridyl acetonitrile (0.2 ml, 1.8 mmol) and **PTH-AB-1CHO** (0.5 ml, 1.8 mmol) were dissolved

in 100 ml of DMF. Piperidine (0.2 ml, 1.8 mmol) was added as a base. The mixture was heated and stirred at 110 °C for 5 hours, and the reaction progress was monitored using TLC. Upon completion, the mixture was separated with chloroform and dried using sodium sulfate. The resulting product was purified through column chromatography (using hexane : ethyl acetate, 8 : 2), yielding a solid-orange product weighing 0.4 g with a 57%. (^{1}H CDCl$_3$, 400 MHz, δ ppm) (Fig. S5†): 8.6 (d, 1H), 8.3 (s, 1H) 6.82 to 7.72 (m, 10H), 6.0 (m, 1H), 5.3 (d, 2H), 4.5 (d, 2H). (^{13}C CDCl$_3$, 101 MHz, δ ppm) (Fig. S6†): 151, 145, 106–146, 51 FT-IR: (KBR, ν/cm^{-1}) (Fig. S7†): 2270. HR-MS (Fig. S9†) calculated for was 367.11, found 367.105.

Results and discussions

Structural characterization

The compound **PTH-AB-PY** was synthesized *via* a three-step reaction, as shown in Scheme 1. In the first step, phenothiazine reacted with allyl bromide in the presence of a sodium hydride base, resulting in the formation of **PTH-AB**. In the subsequent step, **PTH-AB** underwent formylation in the presence of DMF and POCl$_3$, resulting in the formation of **PTH-AB-CHO**. Finally, **PTH-AB-CHO** reacted with 2-pyridyl acetonitrile in the presence of a piperidine base, yielding the desired novel compound (**PTH-AB-PY**).

The synthesized **PTH-AB-PY** was characterized using various analytical techniques. In the ^{1}H NMR spectrum, the disappearance of the aldehyde peak at 9.76 ppm was observed, and a notable singlet appeared at 8.318 ppm, indicating the formation of a vinylene bond (–C=C–). Additionally, a doublet at 8.6 ppm signified the presence of a proton attached to the pyridine nitrogen atom. The corresponding aromatic proton peaks were observed between 6.8 and 7.7 ppm (Fig. S5†). The ^{13}C NMR spectrum indicates the disappearance of the aldehyde carbon peak at 190.44 ppm and the appearance of a vinylene carbon (–C=C–) peak at 149.4 ppm, along with a pyridine carbon connected with N at 151.4 ppm, confirming the formation of the desired product, as shown in (Fig. S6†).

In the FT-IR spectrum, the disappearance of aldehyde –(C–H)– stretching at 2850 and 2900 cm^{-1} clearly indicates the absence of aldehyde, and the formation of 2450 cm^{-1} indicates the formation of nitrile group to confirm the desired

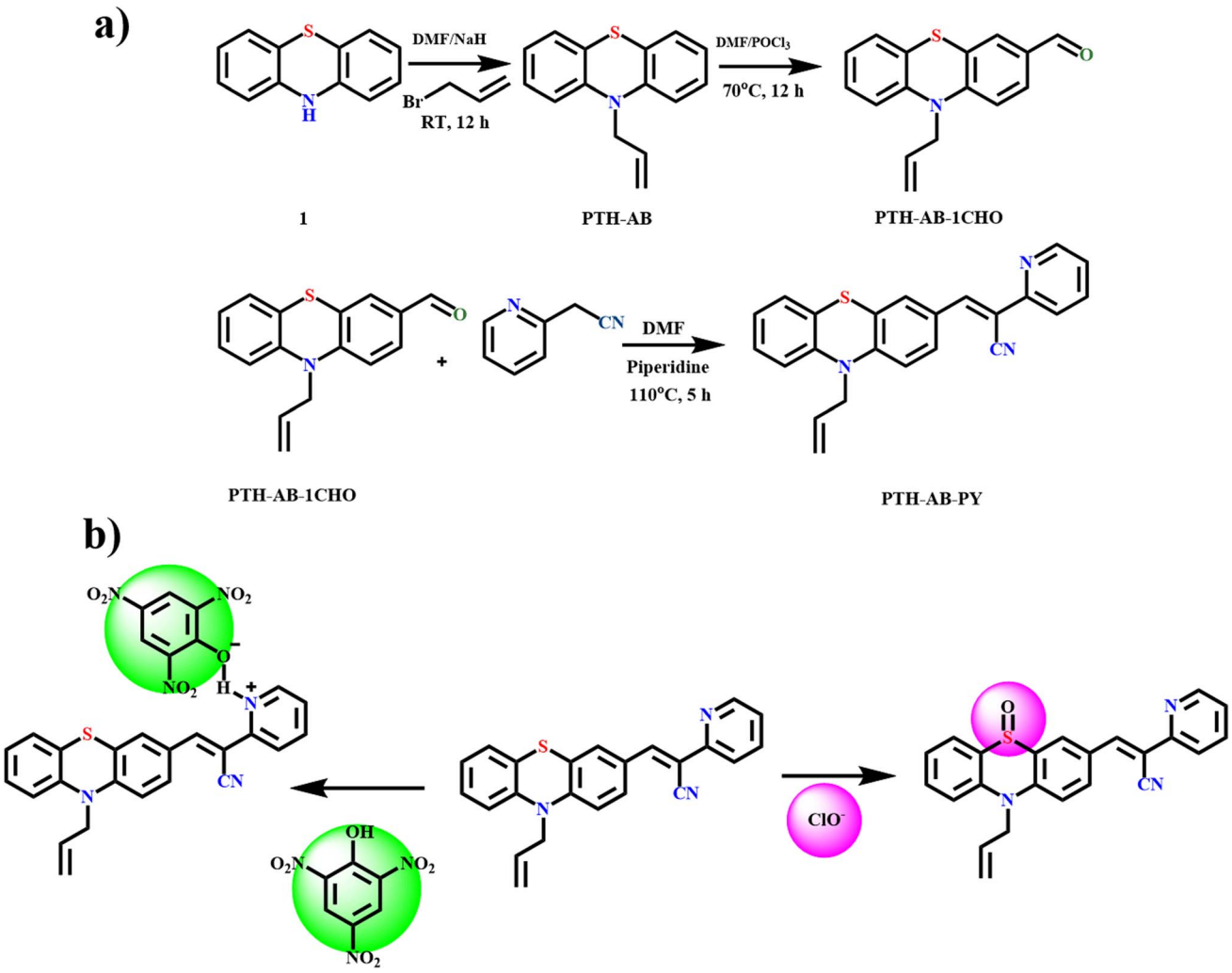

Scheme 1 (a) Synthetic route of target compound PTH-AB-PY. (b) Proposed sensing mechanism of PTH-AB-PY.

compound, as shown in Fig. S7.† In high-resolution mass spectrometry (HRMS), the compound ($C_{23}H_{17}N_3S$) peak was obtained at 365.11 with a 369.11 isotopic peak. It was well agreed to the calculated value of 367.105. The successful synthesis and comprehensive characterization of **PTH-AB-PY** were confirmed by combining data from Fourier-transform infrared spectroscopy (FT-IR), nuclear magnetic resonance (NMR), and high-resolution mass spectrometry (HRMS). This collective evidence forms a strong basis for validating **PTH-AB-PY**.

Crystal description

Single crystal X-ray analysis confirmed the structure of **PTH-AB-PY**. We collected data at 300 K using a D8-QUEST XRD instrument with Mo Kα radiation and applied corrections for Lorentz and polarization effects. The structures were determined using direct methods *via* Olex2-1.5. We obtained a suitable crystal from hexane at room temperature, and crystallization occurred in a monoclinic system (space group $P2_1/n$). The key bond lengths and angles were consistent with the computationally optimized data. The connection between pyridine and phenothiazine occurred at (C1–C2–C4), resulting in a dihedral angle of 122.00(18) degrees. For detailed data, please refer to Tables S1–S3† and the ORTEP diagram (Fig. 1).

Thermal analysis

The thermal stability of the compound was measured using thermo gravimetric analysis in temperatures from 20 °C to 800 °C, as shown in Fig. S8.† It shows significant stability at 250 °C, which indicates the compound will be highly stable with structural properties in high temperatures. In sensor technologies, we need to resist alternations in structure or damage by heat. The resulting stable point shows the compound will remain stable at high temperatures.

Optical properties

The absorption and emission characteristics of **PTH-AB-PY** were investigated in an ACN solution with a concentration of 10^{-4} M, as shown in Fig. 2. Analysis of the compound's absorption spectra displayed two distinctive peaks, the initial peak observed at 320 nm, indicative of π to π* transition, and a second peak at 435 nm, representing an n to π* transition. Upon excitation at 320 nm, the compound exhibited a broad emission peak obtained at 600 nm. The compound shows a higher stock's shift value of around 280 nm.

Solvatochromic properties

We investigated the compound's solvatochromism behavior in different solvents, revealing notable changes. Highly polar solvents showed a significant shift in light absorption towards longer wavelengths. Low polar solvents such as diethyl ether and THF exhibited strong absorption at 418 nm. However, in highly polar solvents like chloroform (427 nm), DMF (425 nm), acetonitrile (419 nm), and ethanol (426 nm), the absorption shifted to higher wavelengths. This trend emphasizes the compound's enhanced light absorption in polar solvents and directly links the solvent's polarity to the stability of the molecule's excited state. Fig. S10† visually illustrates this correlation, showing how various solvent conditions influence the compound's characteristics visually and through spectroscopic data.

AIEE properties

The compound exhibited remarkable Aggregation-Induced Emission Enhancement (AIEE) behavior. The AIEE properties were investigated in THF and water mixtures with varying water percentages from 0 to 90%. Fig. 3(a) shows the fluorescence spectra of **PTH-AB-PY** under different water fractions. Initially, the emission peak for the pure compound appeared at 600 nm. However, a consistent decrease in fluorescence intensity was observed with an increase in water fraction (0% to 70%). Notably, the most significant enhancement occurred at 80% and 90% water fractions, showing an increase in intensity compared to that observed in pure THF (Fig. 3(a)).

This change in intensity resulted in a shift in colour from a light orange (0% wf) to a darker orange shade (80% wf), as shown in Fig. 3(c). However, as the water percentage exceeded 90%, an enhancement in emission intensity was noted, likely due to compound precipitation at higher water concentrations.

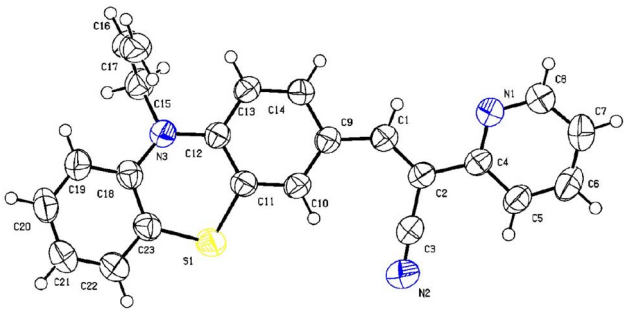

Fig. 1 Crystal structure of PTH-AB-PY.

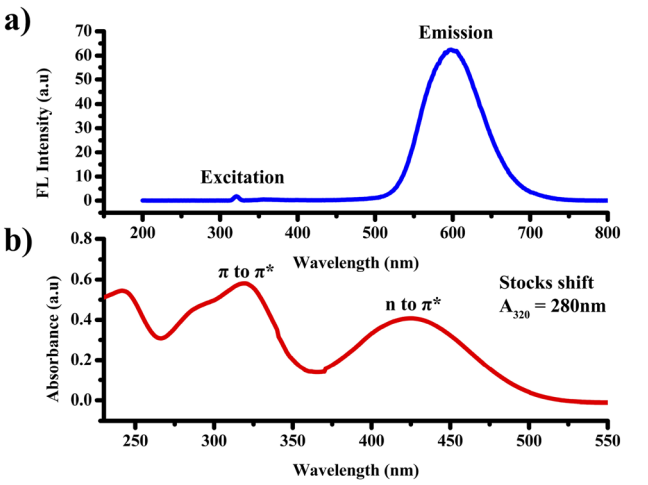

Fig. 2 (a) UV-vis spectrum of PTH-AB-PY. (b) Fluorescence spectrum of PTH-AB-PY.

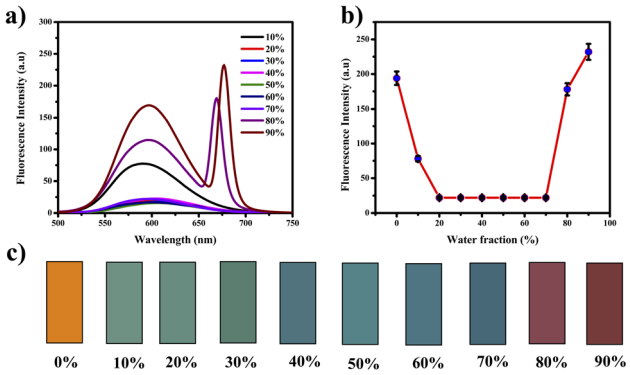

Fig. 3 (a) Fluorescence spectrum of PTH-AB-PY in varying water fraction. (b) Fluorescence emission changes in varying water fractions. (c) Fluorescence colour changes of PTH-AB-PY in different water fractions.

Generally, the shift towards blue or red emission during aggregation corresponds to H-type and J-type aggregation phenomena, respectively. Therefore, the observed 15 nm redshift in the emission maximum at 90% indicates J-type aggregation. The investigation employed scanning electron microscopy (SEM) to analyze the molecules aggregated within a 90% water fraction further and examine structural alterations. In Fig. 4(a), distinct patterns of molecules captured in SEM images provide insights into the modifications occurring within these aggregated molecules. Furthermore, the assessment of particle size distribution Fig. 4(b) of the 90% aggregated compound through SEM analysis revealed an average particle size of 8.9 micrometres.

Sensing behavior of PTH-AB-PY

Anion sensing. We investigated the colorimetric studies of ligand and anion-sensing capabilities in a mixture of acetonitrile and water in a 1 : 1 ratio. The THF : water (20%) solvent mixture exhibited complete quenching in the fluorescence spectrum, leading to the selection of an alternative solvent for further assessment.

The compound (1.8 ml) and 0.2 ml of various anions Cl^-, F^-, COO^-, HCO_3^-, HSO_4^-, I^-, CO_3^{2-}, SO_3^{2-}, Br^-, HPO_4^-, NO_3^-, OH^-, and ClO^- were added.

The compound shows a 65 nm shift towards a higher wavelength (red shift) in the UV spectrum, and a 125 nm shift

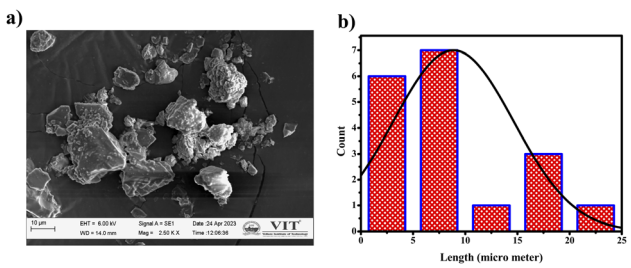

Fig. 4 (a) SEM images of aggregated PTH-AB-PY in 90% water concentration. (b) Particle size distribution of aggregated PTH-AB-PY.

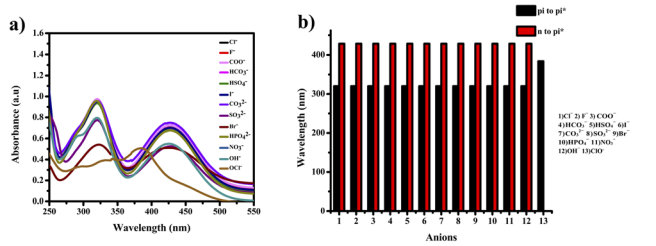

Fig. 5 (a) Selectivity studies and (b) wavelength changes of PTH-AB-PY towards various anions in UV-vis region.

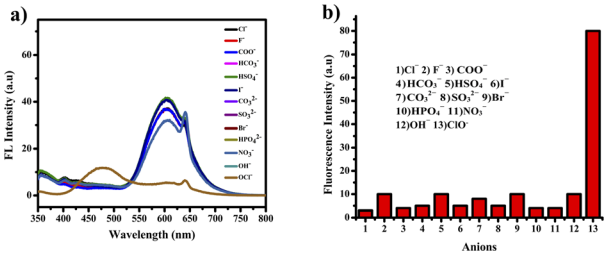

Fig. 6 (a) Selectivity studies and (b) wavelength changes of PTH-AB-PY towards various anions in the FL region.

towards a lower wavelength was observed in the FL spectrum while interaction with ClO^- ions, as shown in Fig. 5(a), (b) and Fig. 6(a), (b). There were no notable changes observed in the other anions. The colorimetric studies are useful for identifying the interactions of the analytes through the naked eye colour change. Here, the colour changes from light orange to colourless obtained in FL light, light greenish to colourless obtained in UV light, and yellow to colourless obtained in visible light, as shown in Fig. 7. The compound shows colour changes in all three light regions. These noticeable colour changes offer an

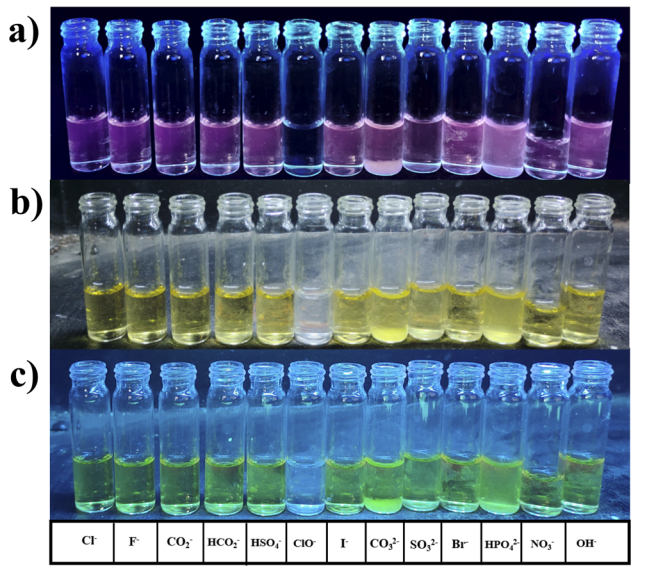

Fig. 7 Optical naked-eye ClO^- sensing towards PTH-AB-PY (a) under FL light. (b) Under UV light. (c) Under visible light.

effective utility for the colorimetric recognition of ClO^- as an oxidizer.

Sensitivity studies. To further confirm the interaction between the compound and ClO^-, we conducted comprehensive studies on the compound's absorption and fluorescence intensity spectra upon adding ClO^- (10 μm). The gradual shifts in wavelength and absorbance correspond to the increase in ClO^- concentration. The absorption band at 320 nm gradually decreased, while a new band formed at 385 nm.

The gradual decrease in the 425 nm band indicated a potential interaction between ClO^- and **PTH-AB-PY**. Isosbestic points observed at 338 nm and 407 nm further supported this interaction. In the fluorescence spectrum, there is a gradual decrease in the 600 nm emission peak and a shift towards a lower wavelength of 475 nm, as shown in Fig. 8(a) and (b). The isosbestic point observed at 548 nm indicates the potential leading to the formation of S=O.

Binding studies. The binding affinity towards compound and ClO^- were measured in Job's plot, as shown in Fig. 10(a)

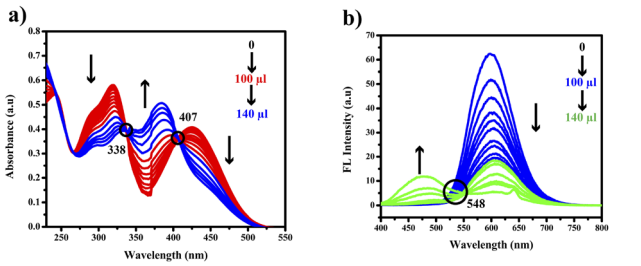

Fig. 8 (a) Titration response of **PTH-AB-PY** in the presence of increasing concentration of OCl^- ions by UV spectroscopy. (b) Titration response of **PTH-AB-PY** in the presence of increasing concentration of OCl^- ions by FL spectroscopy.

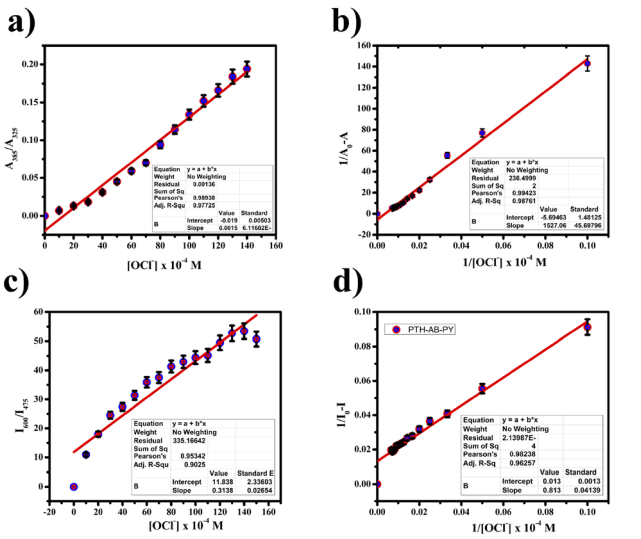

Fig. 9 (a) Ratiometric plots A_{385}/A_{325}. (c) And I_{475}/I_{600}. (b) BH plot of **PTH-AB-PY** in different concentrations of ClO^- in UV-vis spectrum. (d) BH plot of **PTH-AB-PY** in different concentrations of ClO^- in FL spectrum.

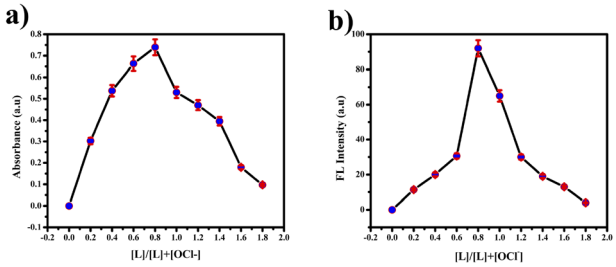

Fig. 10 (a) Job's plot for hypochlorite detection using various concentrations of picric acid in the UV region. (b) FL region.

and (b), observation of absorbance changes occurred at different ClO^- concentrations. The stoichiometric ratio of **PTH-AB-PY** with ClO^- was determined to be 1 : 1 using the Job's plot. We calculated the detection limit (LOD) and quantification limit (LOQ) using the standard formula $K\sigma/s$, where we set K values at 3 for LOD and 10 for LOQ, as depicted in Fig. 9(a) and (c). We established the LOD and LOQ of the novel compound as 6×10^{-4} M and 20×10^{-4} M, respectively. Furthermore, we determined the binding constant by evaluating the intercept/slope ratio based on the observed color change upon adding ClO^- to the compound under UV light and constructing the Benesi–Hildebrand plot using the standard BH formula, as shown in Fig. 9(b) and (d).

We calculated the binding efficiency of ClO^- with the compound as 3.72×10^{-6}, highlighting its excellent binding affinity and selectivity for ClO^-. High-Resolution Mass Spectrometry (HR-MS) confirmed this 1 : 1 ratio by specifically demonstrating the $[\textbf{PTH-AB-PY} + H]^+$ ion with a mass of 385.05, as shown in Fig. S11,† thus ensuring the binding with ClO^-. pH studies ranging from pH 1 to 12 showed no significant changes in the compound's behavior when interacting with ClO^-, as shown in Fig. S12.† Therefore, our compound demonstrates the potential towards ClO^- across various pH conditions. These values surpassed those of other phenothiazine probes, as shown in Table S4,† indicating the exceptional selectivity of the compound, incorporating both phenothiazine and pyridine. The compound demonstrates outstanding specifically for the ClO^- anion (oxidizer).

Nitro aromatics sensing. We evaluated the colorimetric studies of the compound in various nitro aromatics. The addition involved 1.8 ml of the compound and 0.2 ml of nitro

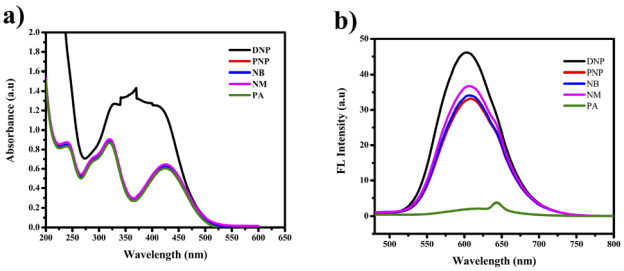

Fig. 11 (a) Selectivity studies of **PTH-AB-PY** towards various nitro aromatics in UV-vis region. (b) FL region.

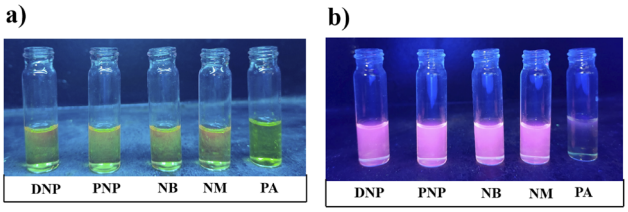

Fig. 12 (a) Discernible colour change upon addition of picric acid to PTH-AB-PY receptor under UV light. (b) FL light.

aromatics. In the UV spectrum, the compound with picric acid shows the merging of π to π* and n to π* bands in the UV-vis spectrum, forming a new band in 360 nm and complete quenching in the FL spectrum, as shown in Fig. 11(a) and (b).

The other nitro aromatics (DNP, PNP, NB, and NM) exhibited no significant changes. Neither the naked eye nor UV light found any color alterations. However, a color change from orange to colorless was observed under FL light, as shown in Fig. 12(a) and (b). This finding demonstrates the ligand's selectivity, incorporating phenothiazine and pyridine, specifically for picric acid (PA).

Sensitivity studies. To further validate the interaction between picric acid and **PTH-AB-PY**, along with the potential formation of a complex involving the oxygen lone pair of picric acid and the pyridine nitrogen of **PTH-AB-PY**, we investigated the absorption and fluorescence intensity spectra of **PTH-AB-PY** upon the addition of picric acid.

Analyzing Fig. 13(a) and (b) revealed notable changes in both wavelength and absorbance as the concentration of picric acid increased. The gradual merging of the two distinct bands led to a new band at 360 nm. We noted a gradual decrease in the 600 nm band in the fluorescence region. This observation suggests the possibility of an interaction between picric acid and **PTH-AB-PY** or the formation of a complex involving the oxygen lone pair of picric acid and pyridine nitrogen.

Binding studies. We determined the limit of detection (LOD) and quantification (LOQ) to be 0.0144×10^{-3} M within the UV region (Fig. 15(a) and (c)), calculated using LOD K values set at 3. Using the standard Benesi–Hildebrand formula, as shown in Fig. 15(b) and (d), we calculated the binding efficiency of picric acid with **PTH-AB-PY** to be 2.4×10^{-3}.

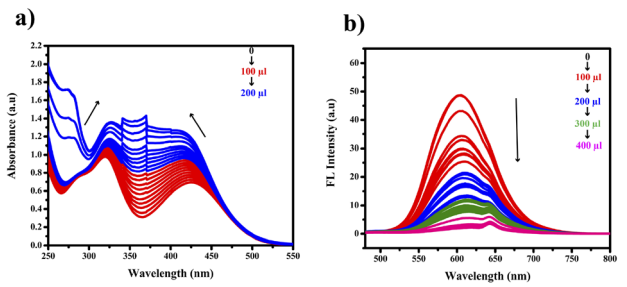

Fig. 13 (a) Titration response of PTH-AB-PY in the presence of increasing concentration of picric acid by UV spectroscopy. (b) Titration response of PTH-AB-PY in the presence of increasing concentration of picric acid by FL spectroscopy.

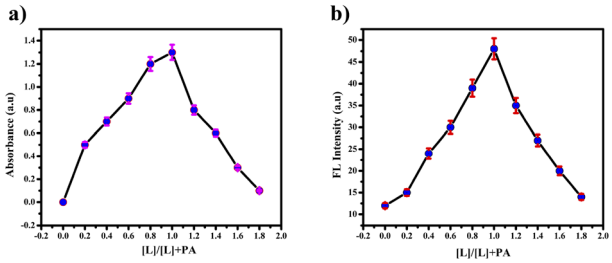

Fig. 14 (a) Job's plot for picric acid detection using various concentrations of picric acid in the UV region. (b) Job's plot for picric acid detection using various concentrations of picric acid in the FL region.

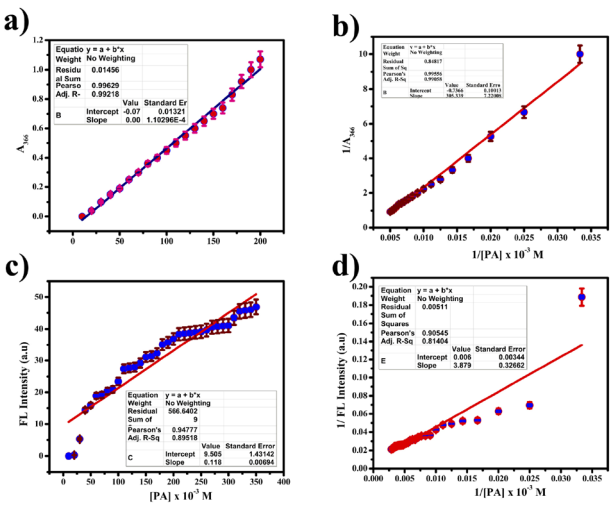

Fig. 15 (a) Ratiometric plots A_{360}. (b) And I_{600}. (c) BH plot of PTH-AB-PY in different concentrations of PA^- in UV-vis spectrum. (d) BH plot of PTH-AB-PY in different concentrations of PA in FL spectrum.

These findings strongly emphasize the ligand's robust binding affinity and selectivity for picric acid. High-Resolution Mass Spectrometry HR-MS (Fig. S13†) and Job's plot (Fig. 14(a) and (b)) notably confirmed the 1 : 1 binding ratio. Specifically, HR-MS demonstrated the presence of the [**PTH-AB-PY** + PA]$^+$ ion with a mass of 597.27, as shown in Fig. S13,† thereby providing clear-cut proof of the interaction between the ligand and picric acid. The assessment of nitroaromatics using **PTH-AB-PY** across various pH levels from 1 to 12 doesn't exhibit significant changes, as shown in Fig. S12.† Therefore, it effectively functions across different pH conditions.

Interference studies. We explored the potential disruption impacts of various anions on accurate hypochlorite detection. To assess this, we monitored changes in the fluorescence intensity emitted by the **PTH-AB-PY**–OCl^- solution upon introducing 12 equivalents of competing anions. These included Cl^-, F^-, COO^-, HCO_3^-, HSO_4^-, I^-, CO_3^{2-}, SO_3^{2-}, Br^-, HPO_4^-, NO_3^-, OH^-, and 5 nitro aromatics. Surprisingly, we observed no significant shifts in spectral changes or variations in emission intensity at 475 in the **PTH-AB-PY**–OCl^- solution. There were no observed changes, as depicted in Fig. 16. This study introduces a dual active probe,

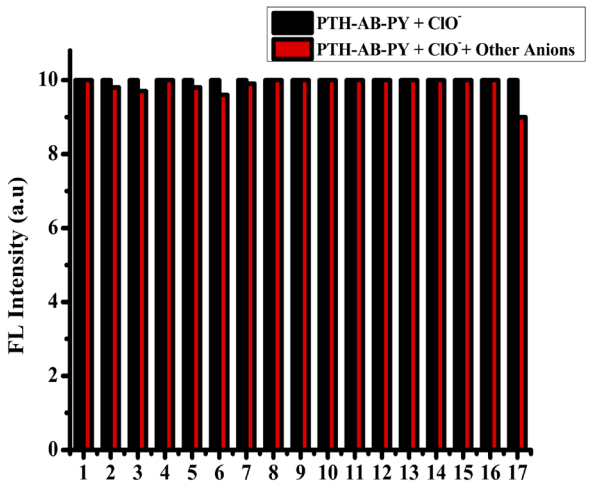

Fig. 16 Interference studies of **PTH-AB-PY** + ClO^- with various anions and nitro aromatics.

making a significant advancement compared to previously reported probes,[37,38] as detailed in Table S4.†

Analytical studies

Test strip analysis. This study used a qualitative analysis to examine the interaction between the ligand and various anions, including chloride, sulfate, and nitrate. We prepared Whatman paper test strips by applying the ligand onto a paper to fabricate this analysis. We observed distinct color changes upon introducing the respective anion solutions to the ligand-coated strips, as shown in Fig. 17(c). The transition from orange to white on the test strip indicated a binding interaction between the ligand and ClO^-. This resulted in a new complex that altered the ligand's optical properties. Additionally, to explore the sensing capabilities of **PTH-AB-PY**, we coated the ligand with silica gel and exposed it to hypochlorite ions (ClO^-). The compound-coated silica gel initially displayed a light orange hue but notably shifted to white upon interacting with ClO^-, as shown in Fig. 17(b). Unfortunately, similar color changes were not observed in the visible and UV-vis regions when examining picric acid.

Real-time water samples and food sample analysis. We evaluated the efficacy of the **PTH-AB-PY** probe to quantify ClO^- and picric acid concentrations in raw water samples obtained from laboratory tap water and the Palar River (Vellore). The collected water samples underwent filtration using 20 nm filter paper to eliminate impurities. Subsequently, ClO^- and the picric acid concentrations ranging from 0 to 20 μl were introduced into the filtered samples. Determining ClO^- and picric acid concentrations involved measuring the emission intensity at 475 nm during excitation, as shown in Fig. 17(a). A standard UV-vis spectrum was a reference to confirm the ClO^- and picric acid concentration in real water samples. By comparing the emission intensities obtained from the water samples with the calibration curve, we estimated the corresponding ClO^- concentrations. The thorough analysis of diverse water samples confirmed the precise identification of the target compound. Crucially, the recovery rates achieved for ClO^- and picric acid detection using the probe ranged from 94.0% to 99%, firmly establishing the efficiency of the probe in the precise and quantitative ClO^- and picric acid detection in real-world water samples (Table S5†). We evaluated the ligand's capability to measure ClO^- and PA levels in various vegetable samples. We extracted the vegetables with water and introduced a known amount of ClO^- and picric acid solutions. Predetermined quantities of ClO^- and PA were introduced into 3 μM probe samples. The calculated recovery values, which approached nearly 99%, affirm the practicality of using **PTH-AB-PY** to accurately determine the amount of ClO^- in various fruit and vegetable samples, as detailed in (Table S6†).

Computational studies

The study utilized the Gaussian 09 program to explore the electronic structure and properties of the investigated system. It found the energy gap (E_{gap}) to be 0.554 eV for the pure compound. However, considering the **PTH-AB-PY** + S=O complex, this gap decreased to 0.454 eV. Comparing the arrangement of atoms between the ligand molecule and the **PTH-AB-PY** + S=O complex revealed noticeable differences. In

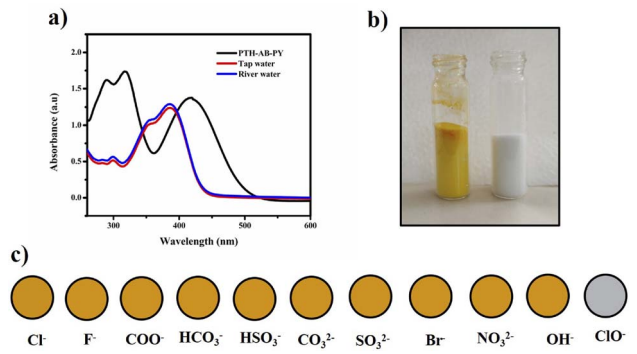

Fig. 17 (a) UV-vis spectra of **PTH-AB-PY** upon addition of ClO^- in tap water and Palar river water. (b) Silica gel-based solid-phase ClO^- detection using **PTH-AB-PY**. (c) Colour change was observed in **PTH-AB-PY** loaded test strips upon the addition of ClO^-.

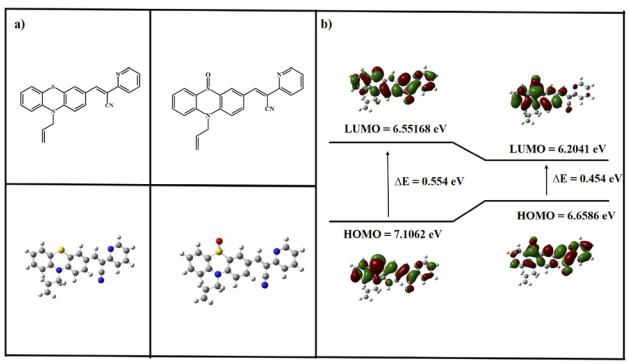

Fig. 18 (a)Theoretically optimized structure of **PTH-AB-PY** and **PTH-AB-PY** + S=O. (b) Frontier molecular orbital (HOMO and LUMO) obtained by **PTH-AB-PY** and **PTH-AB-PY** + S=O DFT-B3LYP and 6-31G.

the **PTH-AB-PY** + S=O complex, electron-absent areas are primarily concentrated in the phenothiazine and pyridine regions, whereas in the ligand, these areas are more prevalent in the phenothiazine section (Fig. 18). Consequently, electron movement within the **PTH-AB-PY** + S=O complex demonstrates clear directionality, primarily flowing from the phenothiazine to the pyridine moiety, whereas in the ligand molecule, electron movement is less distinct. Summing up from the DFT calculations, they indicate that the probe would likely exhibit stronger fluorescence than **PTH-AB-PY** + S=O. This suggests that the fluorescence of **PTH-AB-PY** might diminish upon detecting ClO^-. However, it's impossible to analyze picric acid similarly due to its instability.

Conclusion

The newly synthesized **PTH-AB-PY**, derived *via* Knoevenagel condensation, exhibits remarkable ClO^- selectivity while demonstrating exceptional fluorescence properties. Its comprehensive characterization involved diverse spectroscopic methods, revealing enhanced emission in aggregated molecules observed through scanning electron microscopy. With a high detection limit and a consistent 1 : 1 stoichiometric ratio between **PTH-AB-PY** and ClO^-, the compound demonstrates robust binding efficiency, indicating a strong affinity. Importantly, it shows minimal interference from other reactive oxygen species (ROS) and ensures heightened selectivity specifically for ClO^- detection, evident visually and through fluorescence sensing. Furthermore, the compound displays quenching behavior towards picric acid, showcasing moderate detection limits in both UV and fluorescence regions, rendering it a promising probe for ClO^- and picric acid detection. This distinct conjugated moiety holds substantial promise for various applications, particularly environmental monitoring. Future investigations could further explore its potential applications, emphasizing the importance of designing conjugated moieties for identifying sensitive, reactive oxygen species across various domains.

Author contributions

The manuscript was written by the contributions of all authors.

Conflicts of interest

The authors declare no competing financial interest.

Acknowledgements

The authors gratefully acknowledge VIT University for providing "VIT SEED GRANT" to support this work and for providing the instrumental facilities.

References

1 M. Shafiq, Y. Chen, R. Hashim, C. He, X. Mo and X. Zhou, *Frontiers in Bioengineering and Biotechnology*, 2021, **9**, 821288.
2 J. Tejero, S. Shiva and M. T. Gladwin, *Phys. Rev.*, 2019, **99**, 311–379.
3 A. Vaseashta, M. Vaclavikova, S. Vaseashta, G. Gallios, P. Roy and O. Pummakarnchana, *Sci. Technol. Adv. Mater.*, 2007, **8**(1–2), 47.
4 G. Genchi, A. Carocci, G. Lauria, M. S. Sinicropi and A. Catalano, *Int. J. Environ. Res. Public Health*, 2020, **17**(3), 679.
5 S. Al-Hajj, H. R. Dhaini, S. Mondello, H. Kaafarani, F. Kobeissy and R. G. DePalma, *Frontiers in Public Health*, 2021, **9**, 657996.
6 P. Agarwal, A. Goyal and R. Vaishnav, *Asian J. Pharm. Clin. Res*, 2018, **11**, 27–35.
7 M. Bruze, S. Fregert and B. Gruvberger, Chemical skin burns, in *Handbook of Occupational Dermatology*, Springer, Berlin, Heidelberg, 2000, pp. 325–332.
8 R. J. Ruch, *Toxic Responses of the Skin*, CRC Press, 2020, pp. 133–140.
9 M. D. Igbashio, O. E. Idemudia and H. Ochoyama, *J. Sci. Technol. Res.*, 2022, **4**, 57–71.
10 E. Tskhovrebov, U. Niyazgulov and E. Velichko, *Mater. Sci. Forum*, 2019, **945**, 988–994.
11 Y. B. Barot, V. Anand and R. Mishra, *J. Photochem. Photobiol., A*, 2023, **434**, 114224.
12 D. Svechkarev and A. M. Mohs, *Curr. Med. Chem.*, 2019, **26**, 4042–4064.
13 S. Munusamy, T. R. Mandlimath, P. Swetha, A. G. AlSehemi, M. Pannipara, S. Koppala and R. Boddula, *Environ. Res.*, 2023, **231**, 116046–116046.
14 W. Ahmed, S. L. Simpson, P. M. Bertsch, K. Bibby, A. Bivins, L. L. Blackall and O. C. Shanks, *Sci. Total Environ.*, 2022, **805**, 149877.
15 N. Duan, H. Wang, Y. Li, S. Yang, H. Tian and B. Sun, *Coord. Chem. Rev.*, 2021, **427**, 213557.
16 C. Li, Q. Niu, T. Li, T. Wei, T. Hu, J. Chen and L. Yang, *Dyes Pigm.*, 2020, **180**, 108459.
17 S. Shahim, R. Sukesan, I. Sarangadharan and Y. L. Wang, *Sensors*, 2019, **19**, 1969.
18 J. K. Rajput, *Biosens. Bioelectron.*, 2018, **120**, 153–159.
19 Y. Marcus, *Pure Appl. Chem.*, 1990, **62**, 2069–2076.
20 C. Kalidas, G. Hefter and Y. Marcus, *Chem. Rev.*, 2000, **100**, 819–852.
21 H. Weinberg, A. Galyean and M. Leopold, *TrAC, Trends Anal. Chem.*, 2011, **30**, 72–83.
22 C. W. Isaacson, M. Kleber and J. A. Field, *Environ. Sci. Technol.*, 2019, **43**(17), 6463–6474.
23 Y. Ding, W.-H. Zhu and Y. Xie, *Chem. Rev.*, 2017, **117**, 2203–2256.
24 X. Du and X. Xie, *Sens. Actuators, B*, 2021, **335**, 129368.
25 H. Teymourian, A. Barfidokht and J. Wang, *Chem. Soc. Rev.*, 2010, **49**, 7671–7709.
26 N. Thakur, D. Gupta, D. Mandal and T. C. Nagaiah, *Chem. Commun.*, 2021, **57**, 13084–13113.
27 M. Z. Iqbal, I. Ali, W. S. Khan, X. Kong and E. Dempsey, *Mater. Des.*, 2021, **205**, 109694.
28 C. Liao, M. Zhang, M. Y. Yao, T. Hua, L. Li and F. Yan, *Adv. Mater.*, 2015, **27**, 7493–7527.

29 Y. Yao, R. K. Bennett, Y. Xu, A. M. Rather, S. Li, T. C. Cheung and X. Wang, *Proc. Natl. Acad. Sci. U. S. A.*, 2022, **119**, 2211042119.
30 L. Polavarapu, J. Pérez-Juste, Q. H. Xu and L. M. LizMarzán, *J. Mater. Chem. C*, 2014, **2**, 7460–7476.
31 J. M. Kim, C. Lee, Y. Lee, J. Lee, S. J. Park, S. Park and J. M. Nam, *Adv. Mater.*, 2021, **33**, 2006966.
32 E. Morales-Narváez and A. Merkoçi, *Adv. Mater.*, 2012, **24**, 3298–3308.
33 H. S. Wang, *TrAC, Trends Anal. Chem.*, 2016, **85**, 181–202.
34 Z. Xu and L. Xu, *Chem. Commun.*, 2016, **52**, 1094–1119.
35 A. Kathiravan, M. Narayanan, M. A. Jhonsi and V. Anbazhagan, *Spectrochim. Acta, Part A*, 2023, **303**, 123166.
36 K. Shanmugaraj and S. A. John, *New J. Chem.*, 2018, **42**, 7223–7229.
37 S. Wang, B. Zhu, B. Wang, X. Cao, L. Zhu, J.-T. Hou and L. Zeng, *Chin. Chem. Lett.*, 2021, **32**, 1001–8417.
38 X. Zhong, Q. Yang, Y. Chen, Y. Jiang, B. Wang and J. Shen, *J. Mater. Chem. B*, 2019, **7**, 7332–7337.